Quantum anomalous Hall effect in ferromagnetic transition metal halides

Chengxi Huang,[1,2] Jian Zhou,[2,*] Haiping Wu,[1] Kaiming Deng,[1] Puru Jena,[2,†] and Erjun Kan[1,‡]
[1]*Department of Applied Physics and Key Laboratory of Soft Chemistry and Functional Materials (Ministry of Education), Nanjing University of Science and Technology, Nanjing, Jiangsu 210094, People's Republic of China*
[2]*Department of Physics, Virginia Commonwealth University, Richmond, Virginia 23284, USA*
(Received 19 September 2016; revised manuscript received 16 December 2016; published 10 January 2017)

The quantum anomalous Hall (QAH) effect is a novel topological spintronic phenomenon arising from inherent magnetization and spin-orbit coupling. Various theoretical and experimental efforts have been devoted in search of intrinsic QAH insulators. However, up to now, it has only been observed in Cr or V doped $(Bi,Sb)_2Te_3$ film in experiments with very low working temperature. Based on the successful synthesis of transition metal halides, we use first-principles calculations to predict that the RuI_3 monolayer is an intrinsic ferromagnetic QAH insulator with a topologically nontrivial global band gap of 11 meV. This topologically nontrivial band gap at the Fermi level is due to its crystal symmetry, thus the QAH effect is robust. Its Curie temperature, estimated to be ∼360 K using Monte Carlo simulation, is above room temperature and higher than most two-dimensional ferromagnetic thin films. The inclusion of Hubbard U in the Ru-d electrons does not affect this result. We also discuss the manipulation of its exchange energy and nontrivial band gap by applying in-plane strain. Our work adds an experimentally feasible member to the QAH insulator family, which is expected to have broad applications in nanoelectronics and spintronics.

DOI: 10.1103/PhysRevB.95.045113

I. INTRODUCTION

The discovery of topological insulators (TIs) is one of the most important developments in condensed matter physics during the last decade [1–4]. With its bulk being semiconducting, the edge of a two-dimensional (2D) TI is metallic, showing quantum spin Hall conductivity, protected by time reversal symmetry. An interesting alternate topological quantum matter, quantum anomalous Hall (QAH) effect, arises when the time reversal symmetry is broken intrinsically, usually induced by internal magnetism [5–7]. This was first predicted by Haldane [8]. Subsequently, some 2D materials, such as transition metal (TM) doped TIs [9–11], TM decorated graphene [12,13], Rashba spin-orbit coupling and exchange field induced silicene [14,15], TM based organometallic frameworks [16,17], heavy element layers [18], p-band optical systems [19], noncollinear antiferromagnetic $K_{0.5}RhO_2$ layer [20], and semifunctionalized stanene or germanene [21], are theoretically predicted to possess the QAH effect. In these materials, the spin-orbit coupling (SOC) opens a global band gap at the Fermi level, resulting in a topologically nontrivial insulating property. These QAH insulators are also referred to as Chern insulators, as their topological invariant Chern number is nonzero. In spite of being insulating in the bulk, the QAH insulators feature dissipationless metallic chiral edge states with quantized conductivity, which makes them appealing for high efficiency quantum devices and spintronic applications.

Up to now, the QAH effect has only been experimentally observed in Cr or V doped $(Bi,Sb)_2Te_3$ thin film at very low operation temperature (<85 mK), and the QAH conductance completely vanishes at 2 K [22–24]. For practical interests, one important challenge in synthesizing QAH insulators is to control the distribution of TM atoms, so that weakening of SOC by charge inhomogeneity can be diminished [25,26]. In addition, the synthesis of such thin film is based on molecular beam epitaxy which is expensive and difficult to manipulate. Therefore, search and design of robust and experimentally feasible QAH insulators is important and still ongoing.

Recently, the experimentally synthesized TM^{III} halides [27,28] have received much attention due to their potential applications in spintronics [29]. Due to the weak interlayer van der Waals interactions, these 3D layered crystals can be easily exfoliated down to 2D monolayers [30–32], where the TM atoms are uniformly distributed in a honeycomb structure. While most TM^{III} halide monolayers are discovered to be normal metal or semiconductors [31–33], in this study we find that the ferromagnetic (FM) ruthenium halide (RuX_3, X = Cl, Br, I) monolayers hold the possibility of being topologically nontrivial. Note that previous experimental and theoretical studies have shown that large halogen ligand or in-plane tensile strain can stabilize their FM coupling against antiferromagnetic (AFM) configuration [31,32]. Besides, the SOC effect increases in heavier elements. Hence, here we use the RuI_3 monolayer as an exemplary material to study their electronic and magnetic properties by using first-principles calculations. Our results reveal that the ground state of the RuI_3 monolayer is FM with estimated Curie temperature T_c to be above the room temperature (∼360 K). *Ab initio* molecular dynamics (AIMD) simulations confirm its thermal stability at 500 K. A clear Dirac cone in the spin-down channel appears at the K point in the Brillouin zone near the Fermi level of its band structure. This Dirac cone, due to hybridization of ligand field induced spin-down Ru-e orbitals, is protected by the real space inversion symmetry of the Ru sublattice. After including SOC interactions, the Dirac cone opens a local band gap of 103 meV, showing a topologically nontrivial feature. The system becomes an insulator with a global band gap of 11 meV, in which QAH conductance appears. Thus, we predict that the RuI_3 monolayer is an intrinsic QAH insulator.

*Corresponding author: jzhou2@vcu.edu
†Corresponding author: pjena@vcu.edu
‡Corresponding author: ekan@njust.edu.cn

This QAH effect is robust against any perturbation that keeps the crystal symmetry. The FM configurations of $RuCl_3$ and $RuBr_3$ monolayers are also discussed, where we find similar topologically nontrivial characters at K.

II. COMPUTATIONAL DETAILS

Our first-principles calculations are based on spin-polarized density functional theory (DFT) with generalized gradient approximation (GGA) for exchange-correlation potential given by Perdew, Burke, and Ernzerhof [34] as implemented in the Vienna *Ab initio* Simulation Package (VASP) [35]. A vacuum space of 20 Å along the z direction was adopted to model the 2D system. The projector augmented wave method [36] was used to treat the core electrons, while the valence electrons were represented using a plane-wave basis set. The plane-wave cutoff energy was set to be 500 eV, and the first Brillouin zone was sampled using a Γ-centered $(12\times12\times1)$ Monkhorst-Pack grid [37]. The convergence criteria for energy and force were set to be 10^{-5} eV and 0.01 eV/Å, respectively. The SOC was included in the self-consistent calculations. In order to integrate Berry curvature, a much denser k mesh of $(120\times120\times1)$ was adopted. To verify the GGA results, we also repeated our calculations using the GGA + U method [38], with effective Hubbard U values of 0.5, 1.0, and 1.5 eV for Ru-d electrons. Very similar results have been obtained (Table S2 in the Supplemental Material [39]). We fit a tight-binding Hamiltonian by using maximally localized Wannier functions (MLWFs) [40] to the DFT calculated bands, as implemented in the WANNIER90 package [41].

III. RESULTS

A. Structure and magnetic property of RuI_3 monolayer

Figure 1(a) shows the optimized structure of the RuI_3 monolayer which consists of three flat atomic layers: top-I, middle-Ru, and bottom-I layer. The equilibrium lattice constant of hexagonal lattice is 7.10 Å, larger than that of the $RuCl_3$ monolayer (5.96 Å [42]). Each Ru atom is coordinated to six I atoms with Ru-I bond length of 2.71 Å. The geometric structure is crystallographically subject to the $P\bar{3}1m$ layer group (No. 71). The "thickness" of this monolayer, defined as the distance between the vertical coordinates of the top-I layer and the bottom-I layer, is 3.05 Å. We also calculate its formation energy $E_f = (E_{\mathrm{RuI3}} - 1/4\mu_{\mathrm{Ru}} - 3/4\mu_{\mathrm{I}})$, where E_{RuI3} is the cohesive energy of the RuI_3 monolayer. The chemical potentials μ_{Ru} and μ_{I} are taken from the cohesive energy of the hcp Ru crystal and I_2 molecule, respectively. The calculated formation energy of the RuI_3 monolayer is –0.23eV/atom. This negative value is indicative of an exothermic reaction. The thermal stability is examined by performing AIMD simulations up to 500 K (Fig. S1 in [39]), which implies that the exfoliation reaction to obtain RuI_3 monolayers can be carried out at high temperature.

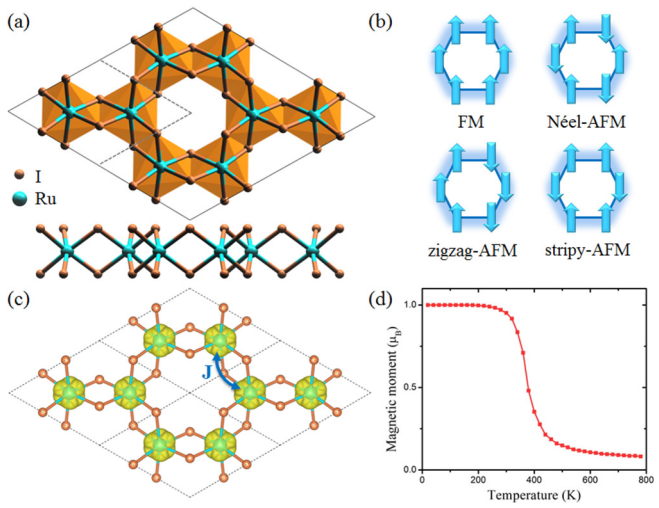

FIG. 1. (a) Top and side views of the optimized 2D RuI_3 monolayer. The dashed rhombus refers to the unit cell. (b) Different magnetic configurations. (c) Spin density (isovalue of 0.04 e/Å^3) and exchange path J. (d) Magnetic moment per formula unit as a function of temperature from Monte Carlo simulation.

Next, we explore the electronic and magnetic properties of the RuI_3 monolayer. Since each I atom needs one electron from Ru (with its valence state of $4d^75s^1$), the formal oxidation state of Ru is +3. This leaves five d electrons on each Ru atom, and our calculation shows that each Ru atom carries $\sim1\mu_{\mathrm{B}}$ magnetic moment. In order to determine the optimal magnetic coupling, we consider four possible magnetic configurations (one FM and three AFM) as shown in Fig. 1(b). We find that the FM state has the lowest total energy [spin density shown in Fig. 1(c)]. The relative energies between the FM and AFM states are listed in Table S1 [39]. During our calculation the Néel-AFM configuration always automatically converged to a nonmagnetic state, whose total energy is higher than that of the FM state by 42 meV per formula unit (RuI_3, denoted as f.u. thereafter). The zigzag-AFM and stripy-AFM states are energetically higher than that of the FM coupling by 20 and 36 meV/f.u., respectively. The FM coupling remains stable when Hubbard U correction is included on the Ru-d electron, but the exchange energy reduces with U (Table S2 in [39] and Ref. [11]). With Hubbard $U = 1.5$ eV, the zigzag-AFM state lies higher than the FM state by 12 meV. This indicates that the estimated Curie temperature will be reduced to ~60%, which should still be observable experimentally under high enough temperature.

To examine the spin dynamical stability against temperature, we use the Ising model to describe the spin Hamiltonian, i.e., $H = -\sum_{\langle ij\rangle} J S_i S_j$, where J refers to the nearest-neighbor exchange parameter [Fig. 1(c)], $S = \frac{1}{2}$ according to our calculation, and the summation runs over all nearest-neighbor Ru. The J is calculated to be 82 meV, with positive value indicating FM exchange coupling. We perform a Monte Carlo simulation to estimate its Curie temperature (T_c). A (20×20) supercell is adopted to reduce translational constraint. The magnetic moment per f.u. is taken after the system reaches an equilibrium state at a given temperature. In Fig. 1(d), we see that T_c is ~360 K, which is above room temperature and higher than those of most 2D FM nanomaterials [43–45].

B. Band structure without including SOC

To gain insight into the electronic properties of the FM RuI_3 monolayer we calculate the electronic band structure and projected density of states (PDOS). Figure 2(a) shows the

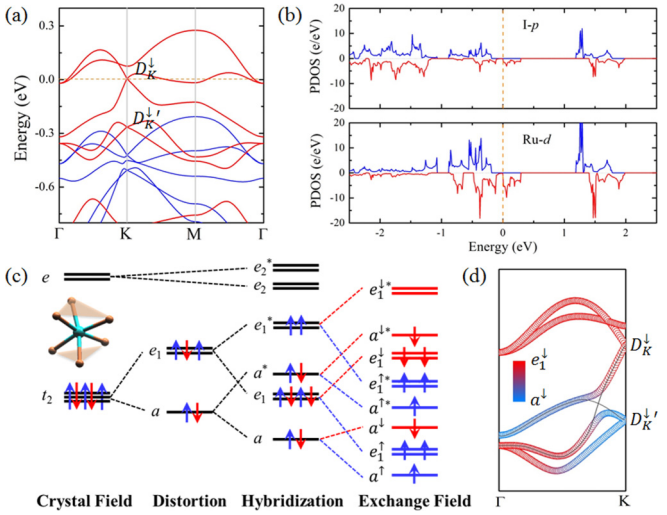

FIG. 2. (a) Band structure without SOC. Blue and red curves represent spin-up and spin-down bands, respectively. (b) Projected density of states. (c) Schematic diagram of the evolution from the atomic d orbitals to the final states at the Γ point. (d) Orbital-resolved spin-down bands around the Fermi level. Different colors represent proportional contributions of $e_1{}^{\downarrow}$ states and $a^{\downarrow}$ states. Thin black curves show the evolution of $e_1{}^{\downarrow}$ and $a^{\downarrow}$ states from Γ to K.

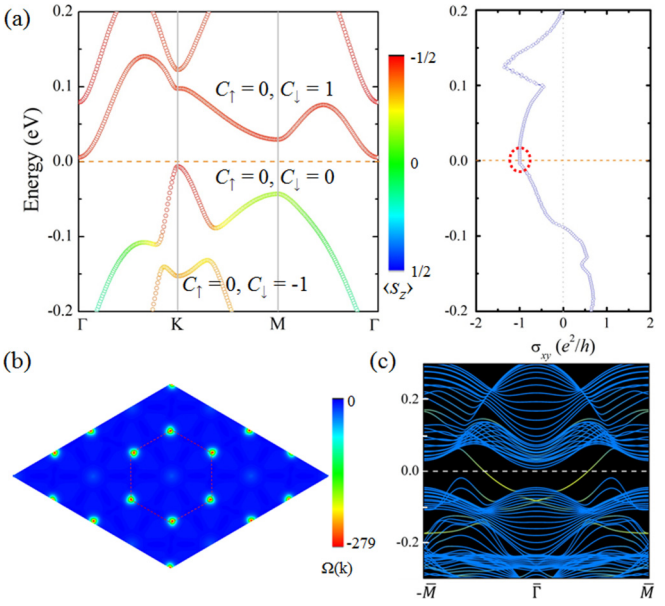

FIG. 3. (a) Band structure with SOC (left panel) and anomalous Hall conductance as a function of the relative chemical potential (right panel). Different colors in the band structure represent the $\langle s_z \rangle$. The Chern numbers of frontier bands are indicated. The quantized terrace of σ_{xy} is highlighted by the red dashed oval. (b) k-resolved Berry curvature $\Omega(k)$. The red dashed hexagon denotes the first Brillouin zone. (c) Tight-binding band structure of nanoribbon obtained by MLWFs show edge states (yellow) inside the gap of bulk bands (blue).

spin-polarized band structure of the FM ground state without including SOC. We find two Dirac cones at the K point in the spin-down channel, denoted as $D_K{}^{\downarrow}$ and $D_K{}^{\downarrow\prime}$. The $D_K{}^{\downarrow}$ is located slightly above the Fermi level ($E_F + 5$ meV with E_F the Fermi energy), and the $D_K{}^{\downarrow\prime}$ is below the Fermi level (E_F–265 meV). From the PDOS [Fig. 2(b)], we see that both these Dirac cones are mainly contributed by Ru-d orbitals.

To better understand the band structure, we start from the d orbitals of a Ru atom [Fig. 2(c)]. Geometrically speaking, each Ru atom is coordinated by six I atoms, forming a distorted octahedral crystal field. In a perfect octahedral crystal field, the five d orbitals split into e and t_2 substates. In this distorted octahedral crystal field, the t_2 further splits into a and e. Hence, the five d orbitals split into three distinct substates, i.e., a, e_1, and e_2 (the little group of the Γ point is D_{3d}). Due to strong ligand field effect, the five Ru^{3+} d electrons occupy only the a and e_1 orbitals, leaving the e_2 empty (distortion step). Furthermore, the hybridizations between two Ru-a and Ru-e_1 orbitals form bonding and antibonding states. In this way, a, e_1, and, a^* orbitals are fully occupied by eight electrons (four spin-up and four spin-down), and the degenerate $e_1{}^*$ states are half-filled by two spin-up electrons, in keeping with the Hund's rule (hybridization step). Such half-filling also implies a stable electron configuration. The exchange between two $e_1{}^*$ orbitals also explains the FM ground state with a magnetic moment of $2\mu_B$ in one unit cell. After incorporating the magnetic exchange field, an energy split occurs between the spin-up and spin-down orbitals. Hence, the $a^{\downarrow *}$ and $e_1{}^{\downarrow *}$ lie higher in energy than the $e_1{}^{\uparrow *}$. This is consistent with the DFT calculated band alignments at the Γ point. Considering the honeycomb lattice of Ru atoms (which contains inversion symmetry of Ru sublattice), the $e_1{}^{\downarrow}$ and $e_1{}^{\downarrow *}$ bands disperse in the momentum space and form the Dirac point $D_K{}^{\downarrow}$ at the K point. Similarly, the dispersion of $a^{\downarrow}$ and $a^{\downarrow *}$ forms the $D_K{}^{\downarrow\prime}$ point. Thus, these Dirac points are protected by crystal symmetry of the Ru sublattice, and are robust against perturbations (such as in-plane strains) which keep its symmetry.

C. SOC induced quantum anomalous Hall effect

Now we turn on the SOC interaction. Since the system has inversion symmetry, there will be no Rashba SOC effect. Because the two bands forming $D_K{}^{\downarrow}$ are contributed by the same irreducible group representation (e), one expects that including intra-atomic SOC ($\mathbf{L}\cdot\mathbf{S}$) would open a large local band gap. Figure 3(a) shows the band structure including SOC, where the degeneracy of $D_K{}^{\downarrow}$ is lifted, opening a direct band gap of 103 meV at K and a global indirect band gap of 11 meV at the Fermi level. A similar band opening also occurs in the $D_K{}^{\downarrow\prime}$ point. Such band gap opening suggests a topologically nontrivial feature at the Fermi level. The out-of-plane spin component $\langle s_z \rangle$ of valence band is slightly quenched. In order to identify its topological property, we calculate the Berry curvature (Ω) and Chern number (C) of each band using a Kubo formula [46,47],

$$C = \sum_{n\in\{O\}} C_n = \frac{1}{2\pi}\int \sum_{n\in\{O\}} \Omega_n(k) d^2k$$
$$= \sum_{n\in\{O\}} (C_{n,\uparrow} + C_{n,\downarrow}),$$

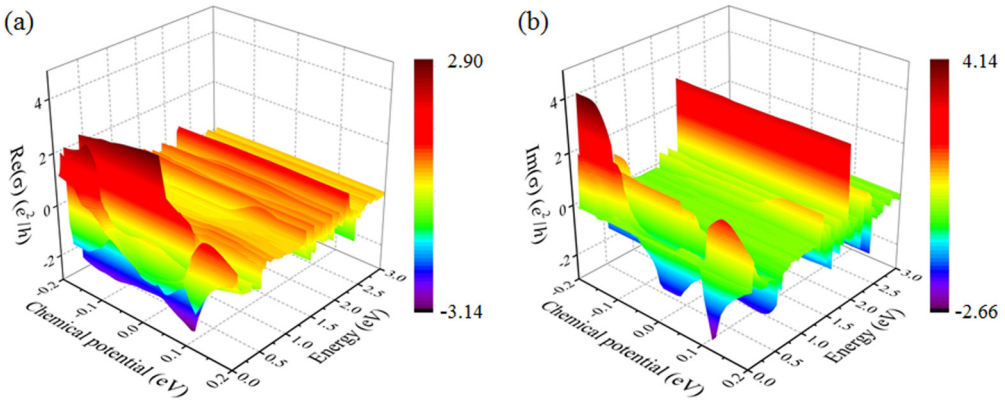

FIG. 4. (a) Real and (b) imaginary parts of the optical conductivity σ_{xy} with respect to photonic energy and chemical potential.

$$\Omega(k) = \sum_{n\in\{O\}} \Omega_n(k) = -2 \sum_{n\in\{O\}} \sum_{n'\neq n} \frac{\mathrm{Im}\,\langle\Psi_{n,k}|v_x|\Psi_{n',k}\rangle\langle\Psi_{n',k}|v_y|\Psi_{n,k}\rangle}{(E_{n,k} - E_{n',k})^2},$$

where n is the band index, $\psi_{n,k}$ is the eigenstate, $v_{x,y}$ is the velocity operator, and $\{O\}$ refers to the occupied band set. The calculated Chern number of each frontier band is indicated in Fig. 3(a). The k-resolved Berry curvature is shown in Fig. 3(b). One clearly sees pronounced positive peaks located at K. Hence, the integration of Berry curvatures for all occupied bands yields a nonzero Chern number $C = -1$, indicating a quantized Hall conductance $\sigma_{xy} = Ce^2/h$ within the bulk band gap. Thus, we demonstrate that the RuI_3 monolayer is a QAH insulator. To be specific, we adjust the chemical potential (relative to the Fermi level) and calculate the anomalous Hall conductance variation, as shown in the right panel of Fig. 3(a). We find a quantized platform of $\sigma_{xy}(-1\times e^2/h)$ within the energy window of the global band gap (11 meV); σ_{xy} gradually decreases when the chemical potential is shifted out of the band gap. Note that the σ_{xy} remains nonzero when the chemical potential lies between –0.1 and +0.2 eV relative to E_F. This large range of nonzero σ_{xy} is different from previous studies where σ_{xy} decreases to zero rapidly out of the energy gap [12,17,48–50]. This would enhance the possibility to observe anomalous Hall conductance in experiments.

One can also confirm the QAH effect by calculating its chiral edge state within the nontrivial band gap. We fit a tight-binding Hamiltonian by using maximally localized Wannier functions to the DFT calculated bands, as implemented in the WANNIER90 package. As shown in Fig. S2 [39], they show very good agreement around the Fermi energy. Without loss of generality, we build a zigzag edged nanoribbon and calculate its band structure using the tight-binding Hamiltonian [Fig. 3(c)]. One clearly sees a metallic edge state appearing in the $\bar{\Gamma} \to \bar{M}$ path (the metallic state in the $-\bar{M} \to \bar{\Gamma}$ path corresponds to the opposite edge of the nanoribbon). Since the Chern number C equals the number of metallic edge states cutting the Fermi level, here we verify that $|C| = 1$.

Motivated by the recent experimental advances in magneto-optical measurement [51] we calculate its optical Hall conductivity to study how the QAH effect evolves in the ac regime. This has not been very well studied in previous computational works and should facilitate the experimental work in the future. The optical Hall conductivity can be written as

$$\sigma_{ac}(\omega) = \frac{e^2}{h} \int \frac{d^2k}{2\pi} \sum_{n'\neq n} (f_{n,k} - f_{n',k}) \times \frac{\mathrm{Im}\,\langle\Psi_{n,k}|v_x|\Psi_{n',k}\rangle\langle\Psi_{n',k}|v_y|\Psi_{n,k}\rangle}{(\omega_{n',k} - \omega_{n,k})^2 - (\omega + i\eta)^2},$$

where $f_{n,k}$ is Fermi-Dirac distribution, ω is incident optical frequency, and η is an infinitesimal parameter. By tuning the chemical potential, we plot the real and imaginary parts of σ_{ac} (Fig. 4), which reflect the reactive and dissipative behavior of an incident photon, respectively. We observe that σ_{ac} strongly fluctuates when $0 < \hbar\omega < 0.5$ eV and $1.3 < \hbar\omega < 2.5$ eV. It almost diminishes when $\hbar\omega$ lies in the range 0.5–1.3 eV, which is mainly due to the large gap between the 0.3 and 1.2 eV in the band structure (Fig. S2 in [39]). In the dc limit ($\omega = 0$), the real part of σ_{ac} is essentially identical to σ_{xy}. The real and imaginary parts of σ_{ac} in the intrinsic state (chemical potential at the Fermi level) are also shown in Fig. S3 [39]. Although the σ_{ac} shows a very complex structure, there are still some features to be noticed. Naively, one expects that the terrace in the optical conductivity immediately vanishes in the ac regime as there is no topological protection. However, in the intrinsic state, the real part of σ_{ac} is around $-1e^2/h$ up to $\hbar\omega = 0.1$ eV. This would help the experimental observation of a large anomalous Hall effect. In the p-doping state (negative relative chemical potential), one always sees a large ac Hall plateau of $\sim 2e^2/h$ at $\hbar\omega = 0.4$ eV, which disappears in the n-doping state.

D. In-plane strain effect

In order to further study the QAH effects of RuI_3, we calculate the in-plane strain effect on magnetic exchange and the global band gap (Fig. 5). We find that, with the nontrivial band topology preserved, a compressive strain increases the bulk band gap, while the tensile strain decreases it. The nontrivial band gap becomes 21 meV when a 2% in-plane compression is applied. On the other hand, the exchange parameter J increases monotonically as the lattice expands. Thus, one can apply an appropriate in-plane strain to achieve an optimal working temperature.

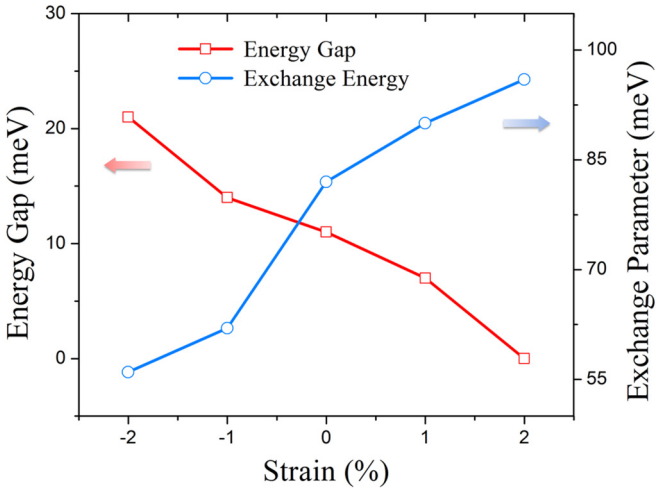

FIG. 5. Nontrivial bulk energy gap and magnetic exchange parameter J as functions of biaxial in-plane strain.

E. Ferromagnetic $RuCl_3$ and $RuBr_3$ monolayers

Besides the RuI_3 monolayer, we also investigate similar $RuCl_3$ and $RuBr_3$ monolayers. Our GGA and GGA + U calculations show that their exchange energies are very small and sensitive to the effective U values. This suggests that the ground states of $RuCl_3$ and $RuBr_3$ monolayers lie at the border between FM and AFM configurations. Hence, in order to achieve robust FM states, one needs to explicitly apply a weak external magnetic field or a small in-plane strain. Nevertheless, we also find similar topological features in FM $RuCl_3$ and $RuBr_3$ monolayers. The calculated band structures of FM $RuCl_3$ and $RuBr_3$ monolayers show similar behavior as the RuI_3 monolayer (Fig. 6). When the SOC is absent, we again find a Dirac point at the K point in the spin-down channel. The SOC lifts the degeneracy of the Dirac point and a nontrivial energy gap opens at K, showing the same nontrivial band topology as in the RuI_3 monolayer. However, in both cases, the conduction band drops below the Fermi level around the Γ point, and the valence band lies above the Fermi level around the M point. Thus both of these materials would show semimetallic features rather than QAH insulating. In spite of this, due to our previous results for the RuI_3 monolayer, one still would observe a chiral dissipationless edge state in their corresponding nanoribbons, and expect that the QAH insulating state can be achieved by applying a weak external magnetic field and/or small in-plane strain.

IV. CONCLUSION

In summary, based on first-principles DFT calculations, we predict that a 2D RuI_3 monolayer is an intrinsic FM QAH insulator. This material could be synthesized in experiments and the TM atoms are uniformly distributed. The Curie temperature is estimated to be ∼360 K, higher than most of the 2D FM thin films studied hitherto. Without including SOC interaction, a Dirac point in the spin-down channel appears at the Fermi level, which is contributed by Ru-d orbitals and protected by the crystal symmetry of the Ru sublattice. The mechanism of such Dirac point has been understood by considering the ligand field effect, hybridization, and magnetic exchange field interactions. Once the SOC is introduced, the symmetry protected Dirac point opens a band gap and

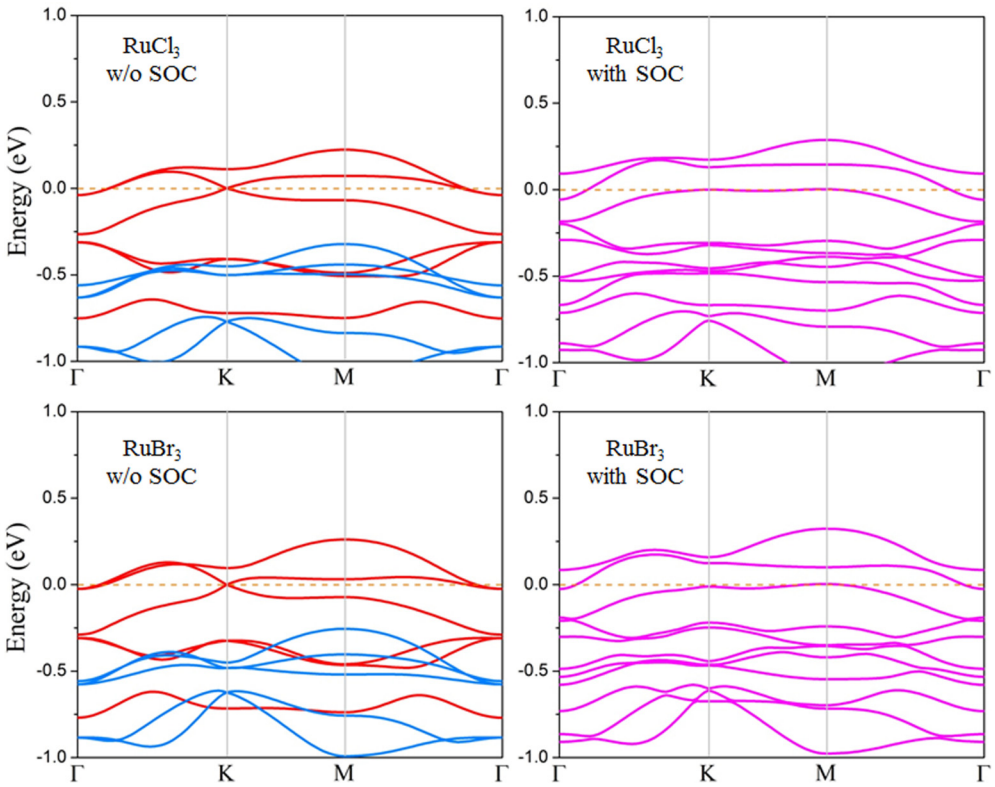

FIG. 6. Band structures of ferromagnetic states for the $RuCl_3$ and $RuBr_3$ monolayers without and with SOC. The blue and red curves in the left panels denote spin-up and spin-down channels, respectively.

the system becomes a QAH insulator with a global band gap of 11 meV. Thus, the topologically nontrivial band gap is robust against perturbations that retain its crystal symmetry. The nontrivial band topology and intrinsic QAH effect are demonstrated by calculating its Berry curvature, Chern number, and chiral edge state. In-plane strain effects are also discussed which are expected to play a role in tailoring both the band gap and the Curie temperature. We look forward to experimental verifications of the QAH effects in the ruthenium halide family.

ACKNOWLEDGMENTS

E.K. is supported by the NSFC (11374160, 51522206, and 11574151), by NSF of Jiangsu Province (BK20130031), by PAPD, the Fundamental Research Funds for the Central Universities (Grant No. 30915011203), and by New Century Excellent Talents in University (NCET-12-0628). C.H. and E.K. acknowledge the support from the Shanghai Supercomputer Centre. P.J. acknowledges support by the U.S. Department of Energy, Office of Basic Energy Sciences, Division of Materials Sciences and Engineering under Award No. DE-FG02-96ER45579. J.Z. and P.J. acknowledge the resources of the National Energy Research Scientific Computing Center supported by the Office of Science of the U.S. Department of Energy under Contract No. DE-AC02-05CH11231. C.H. acknowledges the China Scholarship Council (CSC) for sponsoring his visit to Virginia Commonwealth University (VCU) where this work was conducted.

C.H. and J.Z. contributed equally to this paper.

[1] J. E. Moore, Nature (London) **464**, 194 (2010).
[2] M. Z. Hasan and C. L. Kane, Rev. Mod. Phys. **82**, 3045 (2010).
[3] X.-L. Qi and S.-C. Zhang, Phys. Today **63**(1), 33 (2010).
[4] Y. Ren, Z. Qiao, and Q. Niu, Rep. Prog. Phys. **79**, 066501 (2016).
[5] J. G. Checkelsky, R. Yoshimi, A. Tsukazaki, K. S. Takahashi, Y. Kozuka, J. Falson, M. Kawasaki, and Y. Tokura, Nat. Phys. **10**, 731 (2014).
[6] H. Weng, R. Yu, X. Hu, X. Dai, and Z. Fang, Adv. Phys. **64**, 227 (2015).
[7] C.-X. Liu, S.-C. Zhang, and X.-L. Qi, Annu. Rev. Condens. Matter Phys. **7**, 301 (2016).
[8] F. D. M. Haldane, Phys. Rev. Lett. **61**, 2015 (1988).
[9] R. Yu, W. Zhang, H. J. Zhang, S. C. Zhang, X. Dai, and Z. Fang, Science **329**, 61 (2010).
[10] G. Xu, J. Wang, C. Felser, X.-L. Qi, and S.-C. Zhang, Nano Lett. **15**, 2019 (2015).
[11] S. Qi, Z. Qiao, X. Deng, E. D. Cubuk, H. Chen, W. Zhu, E. Kaxiras, S. B. Zhang, X. Xu, and Z. Zhang, Phys. Rev. Lett. **117**, 056804 (2016).
[12] H. Zhang, C. Lazo, S. Blügel, S. Heinze, and Y. Mokrousov, Phys. Rev. Lett. **108**, 056802 (2012).
[13] Z. Qiao, S. A. Yang, W. Feng, W.-K. Tse, J. Ding, Y. Yao, J. Wang, and Q. Niu, Phys. Rev. B **82**, 161414 (2010).
[14] H. Pan, Z. Li, C.-C. Liu, G. Zhu, Z. Qiao, and Y. Yao, Phys. Rev. Lett. **112**, 106802 (2014).
[15] M. Ezawa, Phys. Rev. Lett. **109**, 055502 (2012).
[16] Z. F. Wang, Z. Liu, and F. Liu, Phys. Rev. Lett. **110**, 196801 (2013).
[17] L. Dong, Y. Kim, D. Er, A. M. Rappe, and V. B. Shenoy, Phys. Rev. Lett. **116**, 096601 (2016).
[18] K. F. Garrity and D. Vanderbilt, Phys. Rev. Lett. **110**, 116802 (2013).
[19] C. Wu, Phys. Rev. Lett. **101**, 186807 (2008).
[20] J. Zhou, Q.-F. Liang, H. Weng, Y. B. Chen, S.-H. Yao, Y.-F. Chen, J. Dong, and G.-Y. Guo, Phys. Rev. Lett. **116**, 256601 (2016).
[21] S.-C. Wu, G. Shan, and B. Yan, Phys. Rev. Lett. **113**, 256401 (2014).
[22] C.-Z. Chang *et al.*, Science **340**, 167 (2013).
[23] X. Kou, S.-T. Guo, Y. Fan, L. Pan, M. Lang, Y. Jiang, Q. Shao, T. Nie, K. Murata, J. Tang, Y. Wang, L. He, T.-K. Lee, W.-L. Lee, and K. L. Wang, Phys. Rev. Lett. **113**, 137201 (2014).
[24] C.-Z. Chang, W. Zhao, D. Kim, Y. H. Zhang, B. A. Assaf, D. Heiman, S.-C. Zhang, C. Liu, M. H. W. Chan, and J. S. Moodera, Nat. Mater. **14**, 473 (2015).
[25] D. Zhang, A. Richardella, D. W. Rench, S.-Y. Xu, A. Kandala, T. C. Flanagan, H. Beidenkopf, A. L. Yeats, B. B. Buckley, P. V. Klimov, D. D. Awschalom, A. Yazdani, P. Schiffer, M. Zahid Hasan, and N. Samarth, Phys. Rev. B **86**, 205127 (2012).
[26] J. Zhang, C.-Z. Chang, P. Tang, Z. Zhang, X. Feng, K. Li, L.-l. Wang, X. Chen, C. Liu, W. Duan, K. He, Q.-K. Xue, X. Ma, and Y. Wang, Science **339**, 1582 (2013).
[27] S. I. Troyanov and E. M. Snigireva, Zh. Neorg. Khim. **36**, 1117 (1991).
[28] H. Bengel, H. J. Cantow, S. N. Magonov, H. Hillebrechtb, G. Thieleb, W. Liang, and M. H. Whangbo, Surf. Sci. **343**, 95 (1995).
[29] A. Banerjee, C. A. Bridges, J.-Q. Yan, A. A. Aczel, L. Li, M. B. Stone, G. E. Granroth, M. D. Lumsden, Y. Yiu, J. Knolle, S. Bhattacharjee, D. L. Kovrizhin, R. Moessner, D. A. Tennant, D. G. Mandrus, and S. E. Nagler, Nat. Mater. **15**, 733 (2016).
[30] V. Nicolosi, M. Chhowalla, M. G. Kanatzidis, M. S. Strano, and J. N. Coleman, Science **340**, 1226419 (2013).
[31] J. Liu, Q. Sun, Y. Kawazoe, and P. Jena, Phys. Chem. Chem. Phys. **18**, 8777 (2016).
[32] W.-B. Zhang, Q. Qu, P. Zhu, and C.-H. Lam, J. Mater. Chem. C **3**, 12457 (2015).
[33] Y. Zhou, H. Lu, X. Zu, and F. Gao, Sci. Rep. **6**, 19407 (2016).
[34] J. P. Perdew, K. Burke, and M. Ernzerhof, Phys. Rev. Lett. **77**, 3865 (1996).
[35] G. Kresse and J. Hafner, Phys. Rev. B **47**, 558 (1993).
[36] P. E. Blöchl, Phys. Rev. B **50**, 17953 (1994).
[37] H. J. Monkhorst and J. D. Pack, Phys. Rev. B **13**, 5188 (1976).
[38] S. L. Dudarev, G. A. Botton, S. Y. Savrasov, C. J. Humphreys, and A. P. Sutton, Phys. Rev. B **57**, 1505 (1998).
[39] See Supplemental Material at http://link.aps.org/supplemental/10.1103/PhysRevB.95.045113 for AIMD simulation results, different magnetic coupling configurations, and a comparison of MLWF and DFT calculated band structures.

[40] N. Marzari, A. A. Mostofi, J. R. Yates, I. Souza, and D. Vanderbilt, Rev. Mod. Phys. **84**, 1419 (2012).
[41] A. A. Mostofi, J. R. Yates, Y.-S. Lee, I. Souza, D. Vanderbilt, and N. Marzari, Comput. Phys. Commun. **178**, 685 (2008).
[42] H.-S. Kim, V. V. Shankar, A. Catuneanu, and H.-Y. Kee, Phys. Rev. B **91**, 241110(R) (2015).
[43] M. Kan, B. Wang, Y. H. Lee, and Q. Sun, Nano. Res. **8**, 1348 (2015).
[44] X. Li, X. Wu, and J. Yang, J. Am. Chem. Soc. **136**, 11065 (2014).
[45] J. Zhou and Q. Sun, J. Am. Chem. Soc. **133**, 15113 (2011).
[46] Y. G. Yao and Z. Fang, Phys. Rev. Lett. **95**, 156601 (2005).
[47] G. Y. Guo, Y. G. Yao, and Q. Niu, Phys. Rev. Lett. **94**, 226601 (2005).
[48] Q.-Z. Wang, X. Liu, H.-J. Zhang, N. Samarth, S.-C. Zhang, and C.-X. Liu, Phys. Rev. Lett. **113**, 147201 (2014).
[49] Z. Qiao, W. Ren, H. Chen, L. Bellaiche, Z. Zhang, A. H. MacDonald, and Q. Niu, Phys. Rev. Lett. **112**, 116404 (2014).
[50] P. Zhou, C. Q. Sun, and L. Z. Sun, Nano Lett. **16**, 6325 (2016).
[51] H. Sumikura, T. Nagashima, H. Kitahara, and M. Hangyo, Jpn. J. Appl. Phys. **46**, 1739 (2007).